PCCP

Accepted Manuscript

ROYAL SOCIETY OF CHEMISTRY

www.rsc.org/pccp

Structural Instability and Mechanical Properties of MoS_2 Toroidal Nanostructures

Jianyang Wu,[1, 2] Gaosheng Nie,[3] Jun Xu,[1] Jianying He, [2] Qingchi Xu,[1, *] Zhiliang Zhang [2, *]

[1]Research Institute for Biomimetics and Soft Matter, Department of Physics, Xiamen University, Xiamen, 361005, China

[2]NTNU Nanomechanical Lab, Department of Structural Engineering, Norwegian University of Science and Technology (NTNU), Trondheim, 7491, Norway

[3]Department of Application Engineering, Jiangxi Normal College, Yingtan, 335000, China

Abstract: Molybdenum disulfide (MoS_2) nanostructures have received considerable research attentions due to their outstanding physical and chemical properties. Recently, a form of MoS_2 ring structure exhibiting unique transport properties has been experimentally identified. Herein, we present the first report describing direct molecular dynamics (MD) simulations of structural instability and mechanical properties of hypothetical MoS_2 nanotube (NT) toroidal nanostructures. Nanorings with small MoS_2 NTs' diameter retain their circular shape because of higher bending stability of NTs, while for those with large diameter of MoS_2 NTs buckling/kinking and displacive phase transformation appear to effectively reduce bending stress as a mechanism for stabilizing the nanorings. However, the nanorings which have to polygonize maintain a circular shape as thick multi-walled inner nanorings are presented. Furthermore, mechanical responses of various nanoweaves (nanochains, nanomailles, and nanochainmailles) by linking nanorings together are also studied. Results show that Young's modulus, stretchability and tensile strength of such nanoweaves depend not only on the helicity of MoS_2 NTs but also the woven pattern. For example, nanostructures

with 4-in-1 weave of nanorings exhibit much higher tensile strength and stiffness but lower extensibility than those with 2-in-1 weave. The finding suggests that MoS_2 NT nanorings and their woven hierarchical structures may be used in the development of new flexible, light-weight electromechanical and optoelectronic nanodevices.

Introduction

The discovery of carbon nanotubes (CNTs) and their extraordinary properties with a variety of promising potential applications have given birth to a new class of materials, known as "one dimensional (1D) tubular nanostructures". This type of nanomaterials has been the subject of intense research in last two decades. Various techniques and strategies have been employed and developed for the production of inorganic non-carbon nanotubes (NTs)[1-5]. Up to now, there have been a large number of polytypes experimentally identified in the case of inorganic nanotubes (INTs)[1-5], such as transition metal chalcogenide (TMC) NTs, transition metal halogenous NTs, oxide NTs, mixed-phase NTs, metal-doped NTs, metal NTs, boron- and silica-based NTs, and so on. Among them, MoS_2 and tungsten disulphide (WS_2) NTs observed shortly after the discovery of the CNTs were the first examples of INTs[6, 7].

These quasi-1D INTs, in analogy to CNTs, are thought of as being formed by rolling up two dimensional (2D) TMC sheets into seamless cylinders. The 2D TMC sheet, rather than being planar graphene, is a tri-layered crystal structure in which the metal layer is sandwiched between the two chalcogen layers with strong metal-sulphur (Mo-S and W-S) covalent bonding. The MoS_2 NT structures have been one of the widely studied INTs because the material is easily available in nature

as molybdenite mineral. The MoS_2 NTs exhibit outstanding electronic properties complementary to CNTs. For instance, a CNT, depending on its chirality and radius, can show either metallic or semiconducting behavior[8] while MoS_2 NTs are all semiconducting nature[9, 10]. As such, an intractable post-processing step is needed to extract semiconducting one from mixed bunches containing both metallic and semiconducting CNTs for serving as building blocks in nanoscale electronics[11], which is different from the case of MoS_2 NTs. MoS_2 NTs also have very intriguing mechanical properties. Experimentally, Kis et al.[12] reported that the shear and Young's modulus of MoS_2 NT ropes are around 0.16 and 120 GPa, respectively, by using a nanobeam configuration. Maharaj and Bhushan[13] conducted both nanoindentation and compression tests on multi-walled MoS_2 NTs to determine their mechanical properties, and it was found that the measured hardness of the MoS_2 NTs was similar to its bulk counterpart while size effect was not observed. Computationally, Kaplan-Ashiri et al[14] predicted the mechanical properties of MoS_2 NTs by means of density-functional tight-binding (DFTB) method. It was found that armchair NT showed diameter-dependent Young's modulus, whereas zigzag NT did not. In contrast, Ansari et al[15] demonstrated a diameter-dependence of Young's modulus for both armchair and zigzag NTs via density functional theory (DFT) calculations. Lorenz et al[16] showed a maximum Young's modulus for both armchair and zigzag MoS_2 NTs when the diameter was 4 nm. But then the Poisson's ratio of zigzag NTs was nearly independent of the diameter while that of armchair NTs was size dependent. A molecular dynamics (MD) study by Zhang et al[17] showed that, for diameters below 7 nm, MoS_2 NTs displayed a diameter- and chirality-dependent anisotropy in elastic response. By using classic MD simulations, Bucholz and Sinnott[18] predicted that the Young's modulus and torsional shear modulus of MoS_2 NTs varied from 211-250 GPa and 73-86 GPa, respectively. Similar to CNTs, MoS_2 NTs tended to buckle subjected to

compression and torsion, and the critical buckling stresses scaled inversely with increasing diameter. CNTs with unique morphological features showed special properties[19-22]. MoS_2, similar to CNTs, also demonstrated the unique ability to form a variety of differing morphological structures with distinct characteristics, such as fullerene-like nanoparticles[23], nanostripes[24], T-shaped NTs[25], helical nanowires[26], nanospirals[27], amorphous nanospheres[28], nanoflowers[29], nanoboxes[30], hierarchical hollow cubic cages[31], and so on. Recently, MoS_2 based ring structures have been synthesized by either catalyzed transport-sonication or thermal evaporation-sulfurization methods[12, 32]. Meanwhile, Fan et al.[32] for the first time reported that the electrical properties of MoS_2 ring were highly sensitive to temperature. When the temperature exceeded 223 K, the measured current increased drastically with the increasing of temperature. Furthermore, an optoelectronic device based on the MoS_2 ring was fabricated with the aid of electron beam lithography (EBL) technique, and it was observed that the as-fabricated device showed both weak field-effect and weak photo-responsive performance as a result of its imperfect structure and unique geometry.

The structural stability and mechanical properties of MoS_2 based rings, which are of importance for the design and fabrication of future devices, have not been explored hitherto, although considerable efforts have been devoted to study the properties of CNT based nanoring structures[33-45]. In the present work, driven by their unique morphology and potential applications, large-scale MD simulations of hypothetical MoS_2 NT nanorings are performed to systematically examine their structural and mechanical properties, focusing on the influences of the helicity, dimension (diameter of NT, diameter of nanoring), and the number of walls present, as well as mechanical behaviors of nanowoven structures (1D nanochains, 2D nanomailles, 3D nanochaimailles) composed of MoS_2 NT

nanorings.

Models and Methodology

In order to generate the atomic model of MoS_2 NT nanorings, finite-length MoS_2 NTs are first built by wrapping-up a 2H-MoS_2 monosheet along a chiral vector. Straight MoS_2 NT is then geometrically folded into a circular ring motif by connecting its ends seamlessly, as shown in Fig. 1. The as-constructed structure is not energetically favorable because of an excessive compression in the inner radius of the nanoring and an excessive tension in the outer radius of the nanoring. In general, a single-walled NT nanoring can be characterized by three geometrical parameters, namely helicity of NTs, radius (r) of NTs and radius (R) of the ring. Previous studies showed that the stability of a defect-free CNT nanoring is primarily dependent on these system parameters[35, 37, 38, 41, 42-44]. To clarify the effects of these parameters, both armchair- and zigzag-type MoS_2 NT nanorings are considered in the simulation. Six armchair-type MoS_2 NT nanorings are constructed with indices of (5,5), (12,12), (20,20), (27,27), (34,34) and (41,41); and (9,0), (22,0), (35,0), (47,0), (59,0) and (71,0) for the zigzag-type nanorings. The corresponding outer diameter of NTs ranges from approximately 1.2 to 7.5 nm. These obtained nanorings are composed of 400 and 232 NT unit cells for armchair and zigzag ones, corresponding to the perimeter of each nanoring about 126 nm. In addition, six lengths of approximately 63, 126, 252, 504, 1008 and 2016 nm of armchair (12,12) and zigzag (20,0) NTs are generated, which allow diameter of nanorings varying from about 20 to 640 nm.

Furthermore, various multi-walled MoS_2 NTs with a constant length around 126 nm are also fabricated to build nanoring. The armchair multi-walled NT nanorings have identical outer wall with indices of (41,41) and the inner walls from (5,5) to (34,34) depending on their number of walls

present, which are referred to as (34,34)@(41,41), (27,27)@(34,34)@(41,41), (20,20)@(27,27)@(34,34)@(41,41), (12,12)@(20,20)@(27,27)@(34,34)@(41,41), and (5,5)@(12,12)@(20,20)@(27,27)@(34,34)@(41,41); the zigzag multi-walled MoS_2 NT nanorings had indices of (59,0)@(71,0), (47,0)@(59,0)@(71,0), (35,0)@(47,0)@(59,0)@(71,0), (22,0)@(35,0)@(47,0)@(59,0)@(71,0), and (9,0)@(22,0)@(35,0)@(47,0)@(59,0)@(71,0). The difference between indices of two adjacent tubes ensures the interwall distances to be roughly 0.57 nm, slightly lower than the thickness of 2D-MoS_2 tri-layer (0.65 nm)[46], which is reminiscent of that multi-walled CNTs have interwall spacing and wall-thickness of 0.3 and 0.34 nm, respectively. The large quintuple-walled MoS_2 NT rings contain 333600 and 338256 atoms for armchair-type and zigzag-type nanorings, respectively.

It was reported that mechanically interlocked molecular systems comprised of ring structures were ideally suited to the construction of artificial nanoscale machines[47, 48]. Accordingly, periodically interlocked 1D nanochains, 2D nanomaille and 3D nanochainmaille are hypothetically constructed by weaving (12,12) or (20,0) MoS_2 NT nanorings together, as illustrated in Fig. 2. The fabrication of such fascinating structures obviates constraint on the sides of nanorings for tensile loading.

Prior to MD simulation, all the free-standing nanoring structures are quasi-statically relaxed to a local minimum energy configuration via the Polak-Ribiere version of conjugate gradient method with an energy tolerance of 1.0×10^{-4} eV and a force tolerance of 1.0×10^{-4} eV/Å. Further MD relaxations are performed with a simulation time of 1 ns under very low temperature T = 0.1 K to eliminate the effect of thermal fluctuations in *NVT* ensemble (constant number of particles, constant volume, and constant temperature) by using Nosé-Hoover thermostat with timestep of 1 fs and a

damping time constant of τ_T = 1 ps. The initial velocities of the atoms in the systems are assigned following the uniform distribution at the given temperature. A non-periodic and shrink wrapped boundary condition is applied along all three axes for isolated nanoring structures, while for the interlocked rings periodic boundary conditions are used along the periodic construction directions. For the mechanical testing of interlocked nanorings, the loadings are simulated by the deformation control technique. The procedure is carried out on the relaxed structures with a reasonable constant strain rate of 10^8 s^{-1} by uniformly rescaling the coordinates of all atoms along the loading directions. This deformation setup corresponds to a *NVT* ensemble in the loading directions. The interlocked structures are able to experience expansion/contraction in the non-periodic directions as a result of the Poisson effect. The atomic stress per atom is calculated based on the virial definition of stress. Atomic potential energy and *von Mises* stress are averaged over 1000 timesteps to eliminate the fast oscillations. All the MD simulations are performed by using the Large-scale Atomic-Molecular Massively Parallel Simulator (LAMMPS) software package[49].

The interatomic interactions are governed by a reactive empirical bond-order (REBO)-type Mo-S forcefield[50, 51], which allows Mo-S bond breaking and formation, and has been utilized for investigation of structural and mechanical properties of MoS_2 nanostructures[52-59]. In detail, this force-field utilizes a bond order potential to determine the short-range interactions coupled with a Lennard-Jones (LJ) term for the long-range van der Waals (vdW) interactions.

Results and Discussion

In a perfect 2D tri-layered MoS_2 sheet, all the Mo-S bonds are identical in length. The length of Mo-S bonds is supposed to vary when the 2D sheet is rolled into a 1D tubular structure. The structural properties of MoS_2 NTs are always associated with their lateral dimension and chiral as CNTs. Structural properties of armchair- and zigzag-type MoS_2 NTs are first investigated by classic MD simulations. Strain energies of a series of MoS_2 NTs are extracted from:

$$E_{strain} = E_{tube} / n(\mathrm{MoS_2}) - E_{unit}(\mathrm{MoS_2})$$

where E_{tube} and $E_{unit}(\mathrm{MoS_2})$ are the total free energy of NT cell and the free energy of a tri-layered MoS_2 unit crystal, and the $n(\mathrm{MoS_2})$ is the number of MoS_2 units in a NT cell. The strain energy E_{strain} reflects the required energy per MoS_2 unit for rolling a 2D MoS_2 sheet into a tube. Fig. 3 presents the strain energy (E_{strain}) against the tube diameter (D). It is readily observed that the calculated E_{strain} is highly dependent on D, following roughly a $1/D^2$ law behavior, which is in accord with a previous DFTB calculation[9]. This nonlinear behavior was also revealed in other known NTs, with the exception of imogolite NT[60]. For small MoS_2 NTs the strain energy is at least one order of magnitude higher than that of CNTs with similar diameter, mainly attributed to more energy required to roll a tri-layered MoS_2 sheet than a mono-layered graphene into a narrow tube. When NTs' diameter is reduced to be less than 4 nm, the strain energy for armchair-type MoS_2 NTs is more favorable than that for zigzag-type as a result of the topologies of the S-Mo-S bonds in different orientations.

MoS_2 NT composed of three mono-atomic S-Mo-S planes implies distinguishable atomic configurations in their outer and inner structures. Structural properties of armchair and zigzag MoS_2 NTs are presented in Fig. 4a-g, where four representative Mo-S bonds are selected as arrow marked

in Fig. 4a and Fig. 4d. It can be seen that the bond lengths and nearest interatomic distances in the outer tube exceed those in the inner tube, resulting from different curvatures of the triple atomic layer structure. Meanwhile, two selected Mo-S bonds in the inner or outer of both armchair and zigzag MoS_2 NT (Fig. 4b and Fig. 4e) are not equivalent in length. The grey line in Fig. 4b and Fig. 4e represents the Mo-S bond length in a 2D MoS_2 sheet. By comparison, the Mo-S bonds in the outer are stretched while those inner are contracted. The degree of the stretching or contracting of Mo-S bonds depends on the tube diameter, following the trend of strain energy. It can be observed from Fig. 4b and Fig. 4e that the zigzag NTs shows stronger size-dependent nearest interatomic distances of Mo‥Mo and outer S‥S than those of armchair ones. It can be summarized that the variations in bond lengths and nearest interatomic distances contribute to the size-dependent strain energy of the NTs.

Geometrically folding straight MoS_2 NTs into ring structures imposes global curvature energy. Fig. 5 shows the evolution path of potential energy per MoS_2 unit during MD relaxation for various MoS_2 NT nanorings, as well as cross-sectional structure of (20,20) and (35,0) NTs of nanorings. It is evident that the energy evolution pathway of MoS_2 NT nanorings is highly related to the diameter of NT. For (5,5), (12,12), (20,20), (9,0), (20,0) and (35,0) chiral NT nanorings, the binding potential energies almost does not vary during MD relaxation. Close inspection on these nanorings reveals that original circular cross-section of (20,20) and (35,0) NTs of nanorings transforms into an elliptical shape after structural relaxation caused by elastic bending (inset of Fig. 5). For the cases of other six large NT nanorings, the binding potential energy density decreases significantly in the early relaxation (0-800 ps), suggesting remarkable structural change in this relaxation stage. Constant

potential energy observed in the late stage of MD relaxation (800-1000 ps) suggests formation of an energetically favorable configuration of NT nanorings.

Specific atomic configuration evolution during the energy relaxation are examined and a series of snapshots of the (41,41) MoS_2 NT nanoring is shown in Fig. 6. A higher binding potential energy level is initially detected in the inner radius of the nanoring due to contraction of the Mo-S bonds and atomic distance (Mo‥Mo and S‥S). Interestingly, there is compensation from the outer radius where a displacive structural transformation (bottom of Fig. 6) take place to remarkably reduce the potential energy as a consequence of artificial extension of atomic distances (Mo‥Mo and S‥S) along zigzag direction. This type of structural transformation was also predicted by Dang et. al.[52, 58] in 2D MoS_2 sheet under nanoindentation. During initial relaxation, excess strain is further released in a wavelike rippling mode along the inner walls. The as-formed ripplocations along with local failures are distinguished from those in bent CNTs where the local ripple buckling can be fully recovered by unconstraint relaxation[61]. A number of local failures in the convex regions of the ripplocations is observed. These ripplocations are metastable and able to further develop during MD relaxation. As is demonstrated at 100 ps, flattening of the NT cross-section is identified. Some local ripple buckling domains distributed along the inner walls extend toward the outer walls. Meanwhile, the phase transformed structures in the outermost walls partially recovers upon stress relief (see three zoomed-in local atomic structures at the bottom of Fig. 6). Subsequently, two buckling develop into localized kinks (200 ps), which facilitates the recovery of NT segments between the kinks (300 ps), in contrast to the case of straight CNTs where the collapsed domain is developed longitudinally over the whole CNT when the diameter of CNTs is over a threshold value which is dependent on the

walls[62, 63]. Further relaxation produces an eventually quadrilateral shaped structure. The sides of the quadrilateral resemble a straightly defective MoS_2 NT. Stress is mostly concentrated in the vicinity of local failures which induces local ripples, as revealed by the highlighted regions in the deformed structure.

Fig. 7 presents snapshots of the (71,0) MoS_2 NT nanoring under delocalized deformations. Close examination of detailed atomic structure shows discrepancies between this zigzag chiral NT nanoring and armchair one in Fig. 6. First, the structural distortion of zigzag (71,0) nanoring is characterized by the appearance of 22 uniformly distributed ripples (10 ps) along the inner side of the nanoring. Unlike the armchair (41,41) nanoring, the appearance of ripples does not involve bond breaking. This suggests that MoS_2 sheet is more prone to structural instability in the zigzag direction than in the armchair direction subjected to compression. Secondly, phase transformation is detected in the middle of the inner walls of zigzag (71,0) nanoring caused by a compression in the armchair direction while it is not observed in (41,41) ring. Likewise, this phase transformation involves a reduction in the $S \cdots S$ intralayer out-of-plane dimension distance. For zigzag (71,0) nanoring formation of buckling does not introduced bond breaking in the structure. Thirdly, the seven buckling (100-400 ps) developed from the ripples ultimately evolve into three deep kinks (1000 ps) distributed along the nanoring, producing a final triangular shaped structure. Phase transformation in the inner walls of nanoring is detected to be partially reversible, being different from that phase transformation in 2D MoS_2 sheet can be fully reversible under release of loading[58]. Typical local atomic structures of zigzag (71,0) nanoring shown in the bottom of Fig. 7 reveal the development of the cross-section of NT of nanorings at the point of the collapse, i.e. from a circular to elliptical, and then to fully

collapsed NT.

The number of walls influences the structural and mechanical properties of NT nanorings. Double- to sextuple-walled MoS_2 armchair and zigzag NT nanorings are investigated and shown in Fig. 8. Apparently, there is a large difference in the ploygonal shapes between multi-walled MoS_2 nanostructures and single-walled one. The main reason is related to a cooperative vdW interaction between neighboring walls in the multi-walled NT nanorings. In a thick multi-walled MoS_2 NT nanoring, all individual nanorings retain their origin circular shape irrespective of chirality of MoS_2 NTs, similar to the case of multi-walled CNT nanoring counterpart[44]. Two main reasons are noted. First, the inner nanorings constrain the outer ones, limiting physical space to develop buckling of nanorings. Secondly, intrinsically high bending stability of the inner NTs made all shells of the NT nanoring difficult to buckle. High energy gradient in armchair-type multi-walled NT nanorings indicates a structural preference of zigzag-type counterpart. To explore in more detail the structural characteristics of multi-walled NT nanorings, locally longitudinal sections of the central part of NT nanorings are captured, as presented in Fig. 9. It is revealed that the chirality of MoS_2 NTs greatly influences not only the buckling onset but also the final buckled configurations. Two locally sharp configurations in the vicinity of the collapsed point of the thin (single- to triple- walled) armchair NT nanorings are in contrast to the smoothly buckled configurations in thin zigzag NT ones. This difference arises from the localized failures occurred in the armchair NT walls while no defects are nucleated near the collapsed points of zigzag NT nanorings. Constant curvature along the entire length of the inner NTs maintains a circular shape of thick armchair NT nanorings, similar to the case of thick zigzag NT nanorings. Cross-sectional shape of MoS_2 NT changes from ellipse to circle as the

thickness of NT walls increase in both type nanorings.

Fig. 10 shows binding potential energy per MoS_2 unit as a function of diameter for (12,12) and (20,0) MoS_2 NT nanorings. In both cases, the potential energy density monotonically decreases with the increase of nanoring diameter, approaching their corresponding constant values of chiral MoS_2 NTs, also similar to the case of (5,5) armchair and (9,0) zigzag CNT nanorings[41]. This suggests an increase in the stored elastic deformation energy density for nanorings with smaller diameter, consistent with the elastic beam theory where the deformation strain energy density (U_{strain}) of a ring structure (diameter D) composed of a hollow cylindrical beam follows as $U_{strain} \propto (1/D)$. A lower potential energy per MoS_2 unit for (12,12) nanoring indicates that the bending rigidity of armchair MoS_2 NT is smaller than that of zigzag NTs except for the case of the smallest nanoring.

Fig. 11 presents the mechanical responses and critical localized configurations of two different 1D nanochains composed of (12,12) and (20,0) nanorings with diameter around 40 nm under uniaxial tension. Strong nonlinear force-strain curves are observed for both nanochains. The two nanochains fail at a force and critical strain of about 7 and 4 nN, 22% and 18%, respectively. However, their complete rupture force and strain reach values close to 110 and 130 nN, 68% and 72%, respectively, while rupture force of 18 nN and maximum strain of 39% for a CNT nanochain under tension were obtained by MD calculation[44]. Prior to the failure, both nanochains show a geometrical change from circular to oval of the rings, resulting in a nonlinear elastic force-strain relationship. The Young's moduli of the MoS_2 nanochains are quantified to be about 2.2 and 2.4 GPa, which are approximately one-tenth of the CNT nanochain[45]. At the stage 1, a drop in stretching force occurs, corresponding to the formation of a frustrated configuration (Fig. 11(a)-1 and (b)-1). Displacive phase transformation

dominates the failure pattern. Failure location at the outer wall of a (12,12) NT nanoring strongly differs with that at the side wall of a (20,0) NT nanoring, reflecting chirality dependent failure mode. As the applied strain increases, another nanoring in the nanochain begins to fail (Fig. 11(a)-2 and (b)-2). Upon the critical strain, buckling of the MoS_2 nanochains appears (Fig. 11(a)-3 and (b)-3), corresponding to a deep drop of the tension force in stage 3 in Fig. 11. This buckling does not involve Mo-S bond breaking. In comparison, the failure zone in the (20,0) NT nanorings of nanochain extends along the NTs. Further stretching leads to collapse of nanochains as a result of forming kinks in nanorings accompanied by a number of Mo-S bond breaking (Fig. 11(a)-4, -5 and (b)-4, -5). Subsequently, the bent NT segments in nanochains between kinks gradually straighten as an augment of elongation, corresponding to a dramatic increase in tension force to their maximum values. Finally, closed nanochains fail by breakage of a nanoring at the kinking sites (Fig. 11(a)-6 and (b)-6), causing a deep drop in force to zero.

Fig. 12 shows the mechanical responses of 2D nanomailles of (12,12) or (20,0) NT nanoring subjected to biaxial straining. The insets of Fig. 12 are instant localized configurations at critical deformations. Due to geometrical symmetry of the nanostructures, the stretching force-strain curves along two perpendicular axes are almost overlapping. The features of force-strain curves are similar to those of 1D nanochains. Three stages can be roughly identified: elastic deformation, elastic-plastic deformation and complete rupture. In the first stage where the strains range up to ~12% and ~10% for (12,12) and (20,0) nanomailles, the tension forces increase monotonically, corresponding to nonlinear elastic deformations. The critical forces (at point number 1 in Fig. 12) are almost identical to those of 1D nanochains, similar to that for a single MoS_2 sheet determined by DFT calculations[53].

However, 2D constructions involve two distinctly mechanical interlocks of nanorings so that the low tangent elastic modulus (~4.4 and ~4.0 GPa) and the critical strains are twice and half large as those of 1D nanochains. This suggests tunable mechanical properties of MoS_2 NT nanostructures via various mechanical interlocks of nanorings. In the second stage, 2D nanomailles fail in a similar pattern to the 1D nanochains, as illustrated in snapshots of number 1, 2, 3, 4 and 5 in Fig. 12. Two distinct morphologies of the nanorings in this deformation stage originate from 2-in-1 and 4-in-1 weaves of nanorings in a unit cell of 2D nanomailles. At high strain (Fig. 12(a)-5 and 12(b)-5), nanorings with 4-in-1 weave square, causing a subsequent increase in tension forces in the curves as a consequence of the elongation and rotation of Mo-S bonds within the straightened MoS_2 NTs. Finally, 4-in-1 woven nanorings completely rupture at forces of ~81 and ~132 nN, and strains of ~42% and ~52% for (12,12) and (20,0) 2D nanomailles, respectively.

Fig. 13 shows the force-strain behaviors of two 3D nanochainmailles under triaxial tension, where the vertical arrows point to the critical strains. As can be seen, the nearly identical mechanical responses along three directions are due to identical pattern of weaves, yet excluding the ultimately complete rupture. The (12,12) and (20,0) 3D nanochaimailles yield at a force of 34 and 18 nN, respectively, which are about five times larger than those of the 1D and 2D nanostructures. The Young's modulus of 3D nanochainmailles evaluated from the initial elastic data are extracted to be 80.9 and 82.8 GPa, which are over tenfold larger than those of 1D and 2D structures. Furthermore, the nanochainmailles show large rupture forces (266 and 216 nN) which are slightly higher than that of a MoS_2 membrane by a nanoindentation measurement[64]. However, their yield and rupture strains are limited to a value of 7.5% and 4.7%, 29% and 27%, respectively. The 4-in-1 woven pattern for all

nanorings in the nanochainmailles is responsible for the robust mechanical properties. The snapshots at the critical strains show that occurrence of deep kinks in nanorings to a large extent releases the compression deformation energy in the inner parts of nanorings, identical to the case of 1D nanochains and 2D nanomailles. As framed by quadrangles in Fig. 13(a)-4, and (b)-4, three individual breakages of nanorings in the 3D nanochaimailles lead to the force drop in the rupture curves along three axis directions.

Conclusions

In summary, based on recent experimentally identified MoS_2 ring structures, toroidal form of various armchair and zigzag-type MoS_2 NT nanorings and their woven nanostructures are hypothetically constructed to investigate their structural instability and mechanical properties by using classic MD simulations with a REBO-type potential. The results show that the armchair MoS_2 NTs are more energetically favorable than the zigzag ones. The energy evolution pathway of MoS_2 NT nanorings with the perimeter of about 126 nm during structural relaxation is closely related to the diameter of NTs. For nanorings with tube diameter less than 4 nm, nanorings experience an elastic deformation during structural relaxation where ovalization of NTs occurs to reduce the bending stress in both outer and inner sides of nanorings. Whereas for those of tube diameter large than 4 nm, nanorings undergo an elastoplastic deformation where buckling, kinking and displacive phase transformation are developed to stabilize the nanorings. In addition, structural morphology, failure mode, and mechanical properties of nanorings are dependent on the chirality and number of the walls in addition to size. Further studies show distinct mechanical properties between 1D nanochains, 2D nanomailles and 3D nanochainmailles. As a result of 4-in-1 weave in 3D nanochainmailles, they

exhibit higher tensile strength and Young's modulus than those of 1D nanochains and 2D nanomailles in which 2-in-1 weave is presented. This suggests that tunable mechanical properties of MoS_2 hierarchical structures can be achieved by interlocking design. This study provides a fundamental understanding of structural and mechanical properties of novel MoS_2 toroidal nanostructures, which sheds light on their future fabrication towards applications in electromechanical, optoelectronics or nanosensor device engineering.

Acknowledgements

This work is supported by the Fundamental Research Funds for the Central Universities (Xiamen University, Grant No. 20720150015, 20720150016 and 20720150017), the National Natural Science Foundation of China (Grant No: 11502221, 21503175 and 21401153) and The Project Sponsored by the Scientific Research Foundation for the Returned Overseas Chinese Scholars, State Education Ministry. The computational resources are provided by the Norwegian Metacenter for Computational Science (NOTUR) at Norwegian University of Science and Technology and Information & Network Center for Computational Science at Xiamen University. We also would like to thank Prof. Douglas E. Spearot from University of Arkansas for sharing the parameters of Mo-S implemented in Large-scale Atomic/Molecular Massively Parallel Simulator (LAMMPS).

*Corresponding Author: xuqingchi@xmu.edu.cn and zhiliang.zhang@ntnu.no.

References

1. R. Tenne, *Front. Phys.*, 2014, **9**, 370.
2. Y. Xiong, B. T. Mayers and Y. Xia, *Chem. Commun.*, 2005, 5013.

3. R. Tenne, *Nat. Nanotechnol.*, 2006, **1**, 103.
4. M. Remškar, *Adv. Mater.,* 2004, **16**, 1497.
5. C. N. R. Rao and A. Govindaraj, *Adv. Mater.*, 2009, **21**, 4208.
6. R. Tenne, L. Margulis, M. Genut and G. Hodes, *Nature*, 1992, **360**, 444.
7. Y. Feldman, E. Wasserman, D. J. Srolovitz and R. Tenne, *Science*, 1995, **267**, 222.
8. P. G. Collins, M. S. Arnold and P. Avouris, *Science*, 2001, **292**, 706.
9. G. Seifert, H. Terrones, M. Terrones, G. Jungnickel and T. Frauenheim, *Phys. Rev. Lett.*, 2000, 85, 146.
10. P. Lu, X. Wu, W. Guo and X. C. Zeng, *Phys. Chem. Chem. Phys*., 2012, 14, 13035.
11. M. C. Hersam, *Nat. Nanotechnol.*, 2008, **3**, 387.
12. A. Kis, D. Mihailovic, M. Remskar, A. Mrzel, A. Jesih, I. Piwonski, A.J. Kulik, W. Benoît and L. Forró, *Adv. Mater.*, 2003, **15**, 733.
13. D. Maharaj and B. Bhushan, *Sci. Rep.*, 2015, **5**, 8539.
14. I. Kaplan-Ashiri, S. R. Cohen, K. Gartsman, V. Ivanovskaya, T. Heine, G. Seifert, I. Wiesel, H. D. Wagner and R. Tenne, *Proc. Nat. Acad. Sci. USA*, 2006, **103**, 523.
15. R. Ansari, S. Malakpour, M. Faghihnasiri and S. Sahmani, *Superlattice Microst*., 2015, **82**, 188.
16. T. Lorenz, D. Teich, J.-O. Joswig and G. Seifert, *J. Phys. Chem. C*, 2012, **116**, 11714.
17. D.-B. Zhang and T. Dumitrică, *Phys. Rev. Lett.*, 2010, **104**, 065502.
18. E. W. Bucholz and S. B. Sinnott, *J. Appl. Phys.*, 2012, **112**, 123510.
19. J. H. Zhao, J. Y. Wu, J-.W. Jiang, L. X. Lu, Z. L. Zhang and T. Rabczuk, *Appl. Phys. Lett.*, 2013, **103**, 233511.
20. J. Y. Wu, J. Y. He, G. M. Odegard, S. Nagao, Q. S. Zheng, and Z. L. Zhang, *J. Am. Chem. Soc.*, 2013, **135**, 13775.
21. J. Y. Wu, J. Y. He and Z. L. Zhang, *Comput. Mater. Sci.*, 2013, **80**, 15.
22. J. Y. Wu, S. Nagao, J. Y. He and Z. L. Zhang, *Small*, 2013, **9**, 3561.
23. M. Chhowalla and G. A. Amaratunga, *Nature*, 2000, **407**, 164.
24. S. Wang, C. An and J. Yuan, *Materials*, 2010, **3**, 401.
25. R. Tenne, M. Homyonfer and Y. Feldman, *Chem. Mater.*, 1998, **10**, 3225.
26. F. L. Deepak, R. Esparza, B. Borges, X. López-Lozano and M. Jose-Yacaman, *Catal. Lett.*, 2011, **141**, 518.
27. L. Zhang, K. Liu, A. B. Wong, J. Kim, X. Hong, C. Liu, T. Cao, S. G. Louie, F. Wang and P. Yang, *Nano Lett.*, 2014, **14**, 6418.

28. Y. Tian, X. Zhao, L. Shen, F. Meng, L. Tang, Y. Deng and Z. Wang, *Mater. Lett.*, 2006, **60**, 527.
29. Z. Hu, L. Wang, K. Zhang, J. Wang, F. Cheng, Z. Tao and J. Chen, *Angew. Chem. Int. Ed.*, 2014, **126**, 13008.
30. A. W. Maijenburg, M. Regis, A. N. Hattori, H. Tanaka, K.-S. Choi and J. E. ten Elshof, *ACS Appl. Mater. Interfaces*, 2014, **6**, 2003.
31. L. Ye, C. Wu, W. Guo and Y. Xie, *Chem. Commun.*, 2006, 4738.
32. C. Fan, T. Li, Z. Wei, N. Huo, F. Lu, J. Yang, R. Li, S. Yang, B. Li, W. Hu and J. Li, *Nanoscale*, 2014, **6**, 14652.
33. M. Zheng and C. Ke, *Small*, 2010, **6**, 1647.
34. B. J. Cox and J. M. Hill, *J. Phys. Chem. C*, 2007, **111**, 10855.
35. O. Hod, E. Rabani and R. Baer, *Phys. Rev. B*, 2003, **67**, 195408.
36. N. Xu, J.-W. Ding, M.-M. Ma and X. Tang, *Chin. Phys. B*, 2010, **19**, 0161016.
37. L. Liu, C. S. Jayanthi and S. Y. Wu, *Phys. Rev. B*, 2001, **64**, 033412.
38. P. Liu, Y. W. Zhang and C. Lu, *J. Appl. Phys.*, 2005, **98**, 113522.
39. Z. Zhang, J. Yuan, M. Qiu, J. Peng and F. Xiao, *J. Appl. Phys*., 2006, **99**, 104311.
40. P. Liu and Y. W. Zhang, *Carbon*, 2010, **48**, 2225.
41. I-L., Chang and J.-W. Chou, *J Appl. Phys.*, 2012, **112**, 063523.
42. C. Chen, J.-G. Chang, S.-P. Ju and C.-C. Hwang, *J. Nanopart. Res.*, 2011, **13**, 1995.
43. C. Pozrikidis. *Comput. Mater. Sci.*, 2008, **43**, 943.
44. P. Liu, Y. W. Zhang and C. Lu, *Phys. Rev. B*., 2005, **72**, 115408.
45. N. Chen, M. T. Lusk, A. C. T. van Duin and W. A. Goddard III, *Phys. Rev. B*, 2005, **72**, 085416.
46. R. F. Frindt, *J. Appl. Phys.*, 1966, **37**, 1928.
47. D. A. Leigh, J. K. Y. Wong, F. ois Dehez and F. Zerbetto, *Nature*, 2003, **424**, 174.
48. J. Lu, D. R. Turner, L. P. Harding, L. T. Byrne, M. V. Baker and S. R. Batten, *J. Am. Chem. Soc*. 2009, **131**, 10372.
49. S. J. Plimpton, *J. Comput. Phys*., 1995, 117, 1.
50. T. Liang, S. R. Phillpot and S. B. Sinnott, *Phys. Rev. B*, 2009, **79**, 245110.
51. T. Liang, S. R. Phillpot and S. B. Sinnott, *Phys. Rev. B*, 2012, **85**, 199903-4(E).
52. K. Q. Dang and D. E. Spearot, *J. Appl. Phys.,* 2014, **116**, 013508.
53. S. Xiong and G. Cao, *Nanotechnology*, 2015, **26**, 185705.

54. S. K. Singh, M. Neek-Amal, S. Costamagna and F. M. Peeters, *Phys. Rev. B*, 2015, **91**, 014101.

55. E. W. Bucholz and S. B. Sinnott, *J. Appl. Phys*., 2012, **112**, 123510.

56. J. A. Stewart and D. E. Spearot, *Modelling Simul. Mater. Sci. Eng*., 2013, **21**, 045003.

57. X. Wang, A. Tabarraei and D. E. Spearot, *Nanotechnology*, 2015, **26**, 175703.

58. K. Dang, J. Simpson and D. Spearot, *Scr. Mater.*, 2014, **76**, 41.

59. D.-M. Tang, D. G. Kvashnin, S. Najmaei, Y. Bando, K. Kimoto, P. Koskinen, P. M. Ajayan, B. I. Yakobson, P. B. Sorokin, J. Lou and D. Golberg, *Nat. Commun.*, 2014, **5**, 3631.

60. L. Guimarães, A. N. Enyashin, J. Frenzel, T. Heine, H. A. Duarte and G. Seifert, *ACS Nano*, 2007, **1**, 362.

61. A. Kutana and K. P. Giapis, *Phys. Rev. Lett.*, 2006, **97**, 245501.

62. T. Chang, *Phys. Rev. Lett.,* 2008, **101**, 175501.

63. N. G. Chopra, L. X. Benedict, V. H. Crespi, M. L. Cohen, S. G. Louie and A. Zettl, *Nature*, 1995, **377**, 135.

64. S. Bertolazzi, J. Brivio and A. Kis. *ACS Nano*, 2011, **5**, 9703.

Figure Captions

Figure 1. Atomic model of a MoS_2 NT nanoring generated by geometrically bending an initially straight MoS_2 NT.

Figure 2. Schematics of 1D nanochain, 2D nanomaille and 3D nanochainmaille constructed by orderly weaving MoS_2 NT nanorings. One unit cell of these 1D, 2D and 3D nanostructures contains 2, 3, 5 nanorings, respectively.

Figure 3. Strain energy per MoS_2 unit as a function of tube diameter and the inset illustrate curvature change as rolling a sheet into a tube.

Figure 4. Structural properties of MoS_2 NTs. (a) Top-view of structural configuration of (10,10) MoS_2 NT where representative bonds are marked. (b) and (c) Representative Mo-S bond length and atomic nearest distance against the diameter of armchair-type NTs, respectively. (d) Top-view of structural configuration of (20,0) MoS_2 NT where representative bonds are marked. (e) and (f) Representative Mo-S bond length and atomic nearest distance against the diameter of zigzag-type NTs, respectively.

Figure 5. Evolution of potential energy per MoS_2 unit for (a) various armchair and (b) zigzag NT nanorings during MD relaxation time of 1000 ps, together with snapshots of cross-section of (20,20) and (35,0) NTs of nanorings.

Figure 6. Top-view snapshots of (41,41) NT nanoring at various MD simulation stages, as well as local outer structures of nanoring for identifying structural transformation. Atoms are colored according to the potential energy.

Figure 7. Top-view snapshots of (71,0) NT nanoring at various MD simulation stages, as well as

side-view of the NT for monitoring the evolution of the nanoring at the point of the collapse. Atoms are colored according to the potential energy.

Figure 8. Top-view snapshots of double- to sextuple-walled NT nanorings at MD simulation of 1000 ps, (a) armchair and (b) zigzag. Atoms are colored according to the potential energy.

Figure 9. Close-view of longitudinal sections of the central part of multi-walled NT nanorings, (a) armchair and (b) zigzag, where multi-walled NTs are individually painted with different color for clarification.

Figure 10. Potential energy per MoS_2 unit as a function of diameter of (12,12) and (20,0) MoS_2 NT nanorings.

Figure 11. Mechanical responses of 1D nanochains constructed by (a) (12,12) and (b) (20,0) MoS_2 NT nanorings subjected to uniaxial tension. Several localized configurations are captured at critical deformation stages marked in the zoomed-in force-strain curves. Atoms are colored according to their potential energy.

Figure 12. Mechanical responses of 2D nanomailles constructed by (a) (12,12) and (b) (20,0) MoS_2 NT nanorings subjected to biaxial tension. Red and black lines denote the data measured along the two in-plane directions. Several localized configurations are captured at critical deformation stages marked in the zoomed-in force-strain curves. Atoms are colored according to their potential energy.

Figure 13. Mechanical responses of 3D nanochainmailles constructed by (a) (12,12) and (b) (20,0) MoS_2 NT nanorings subjected to triaxial tension. Red, green and black lines denote the data measured along the *x*, *y*, and *z* directions, respectively. Four localized configurations are captured at

critical deformation stages marked in the stretching force-strain curves. Atoms are colored according to their potential energy. Rectangular frames point to the separations of the nanorings caused by rupture.

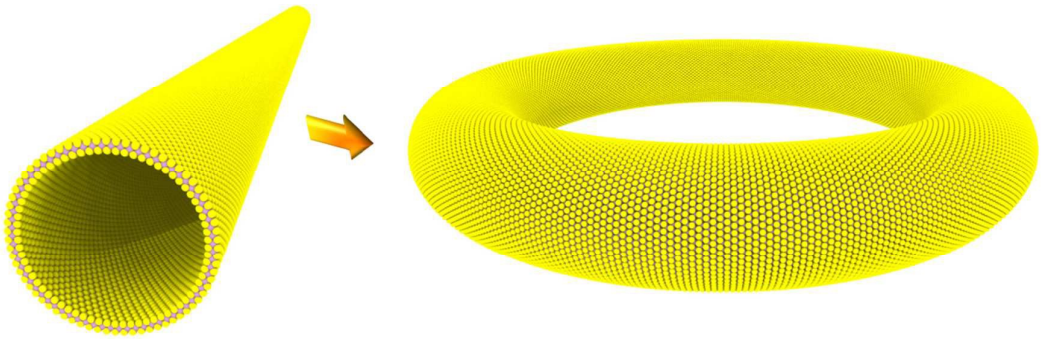

Figure 1

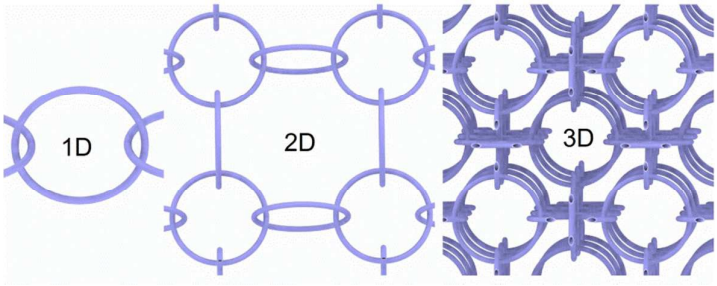

Figure 2

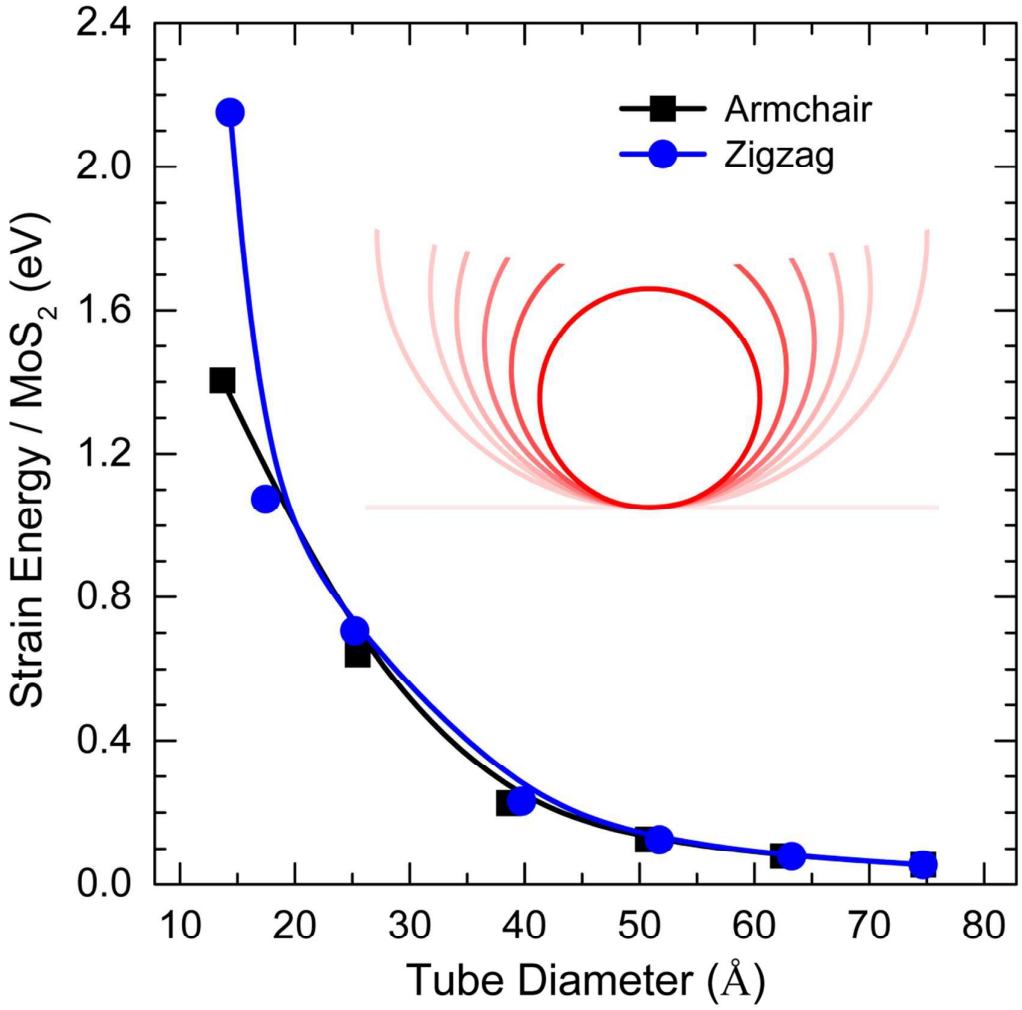

Figure 3

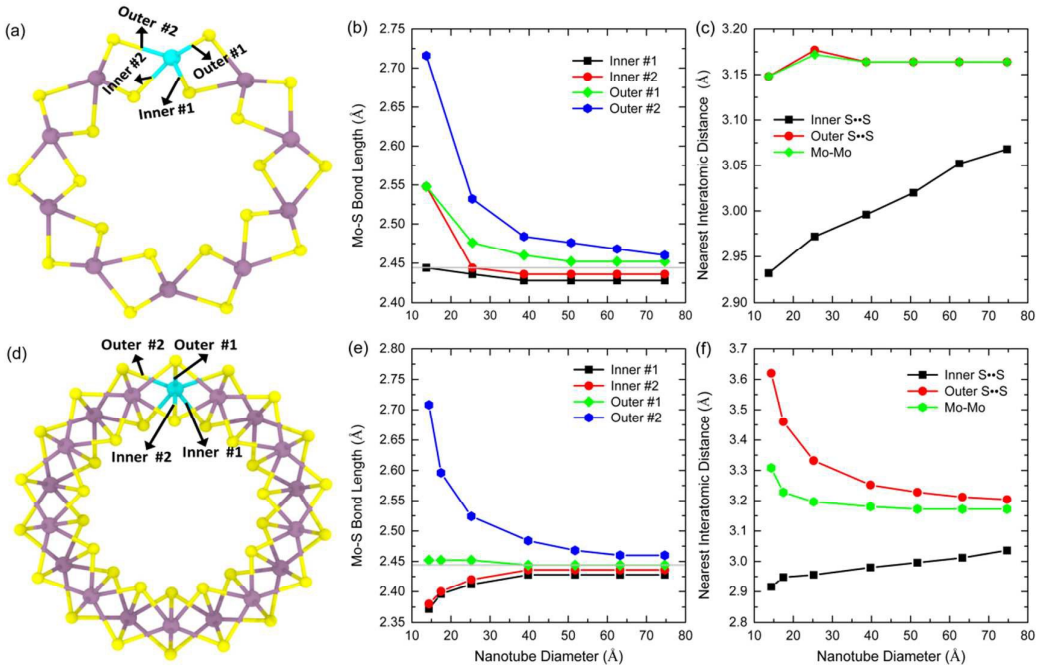

Figure 4

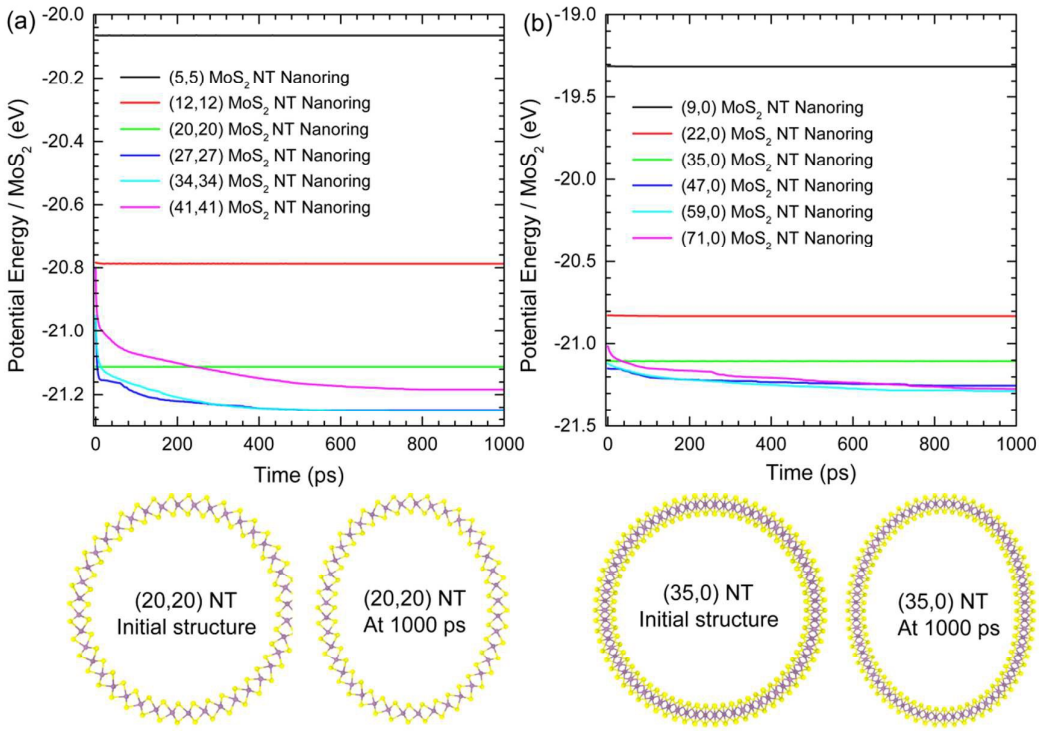

Figure 5

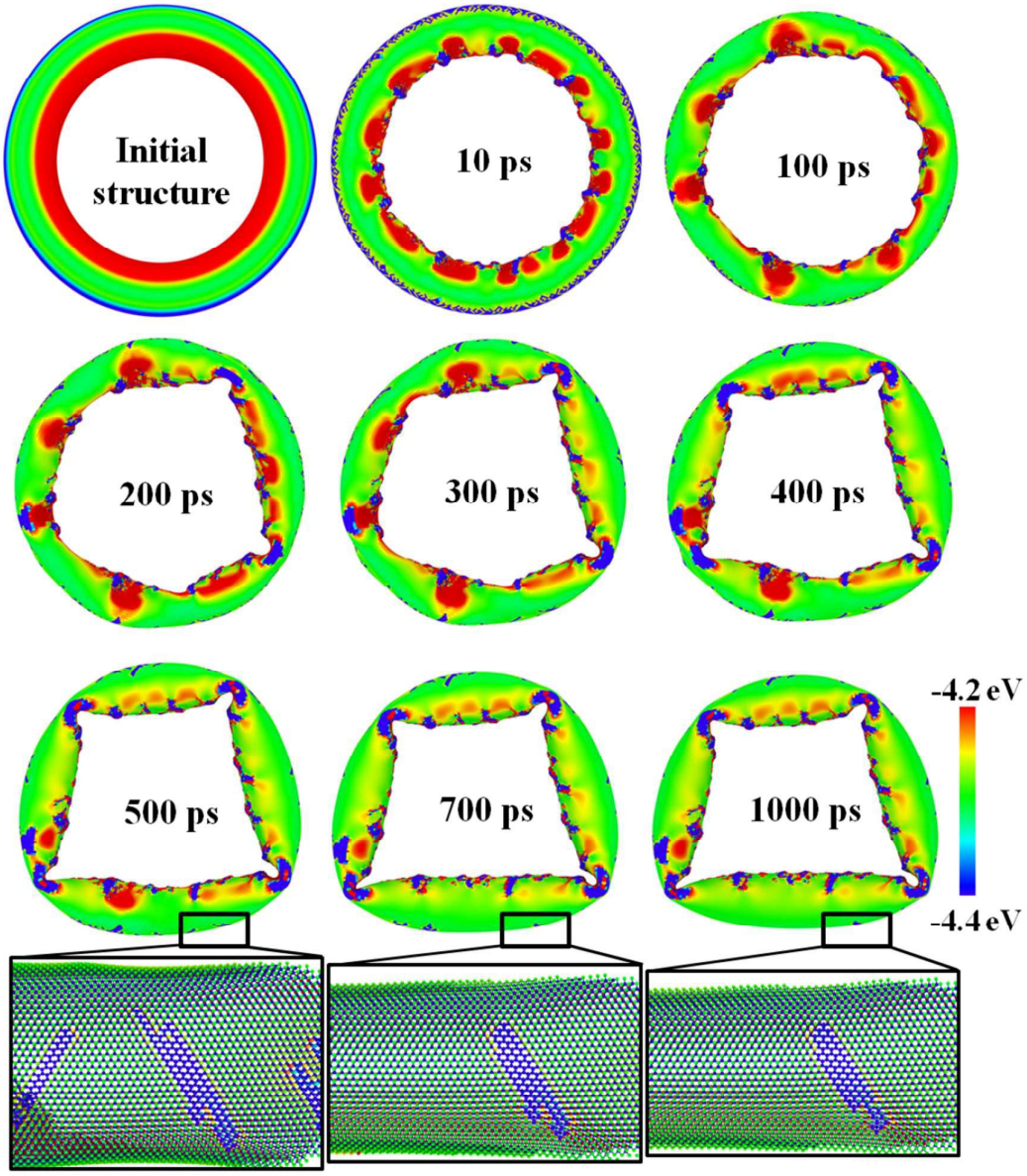

Figure 6

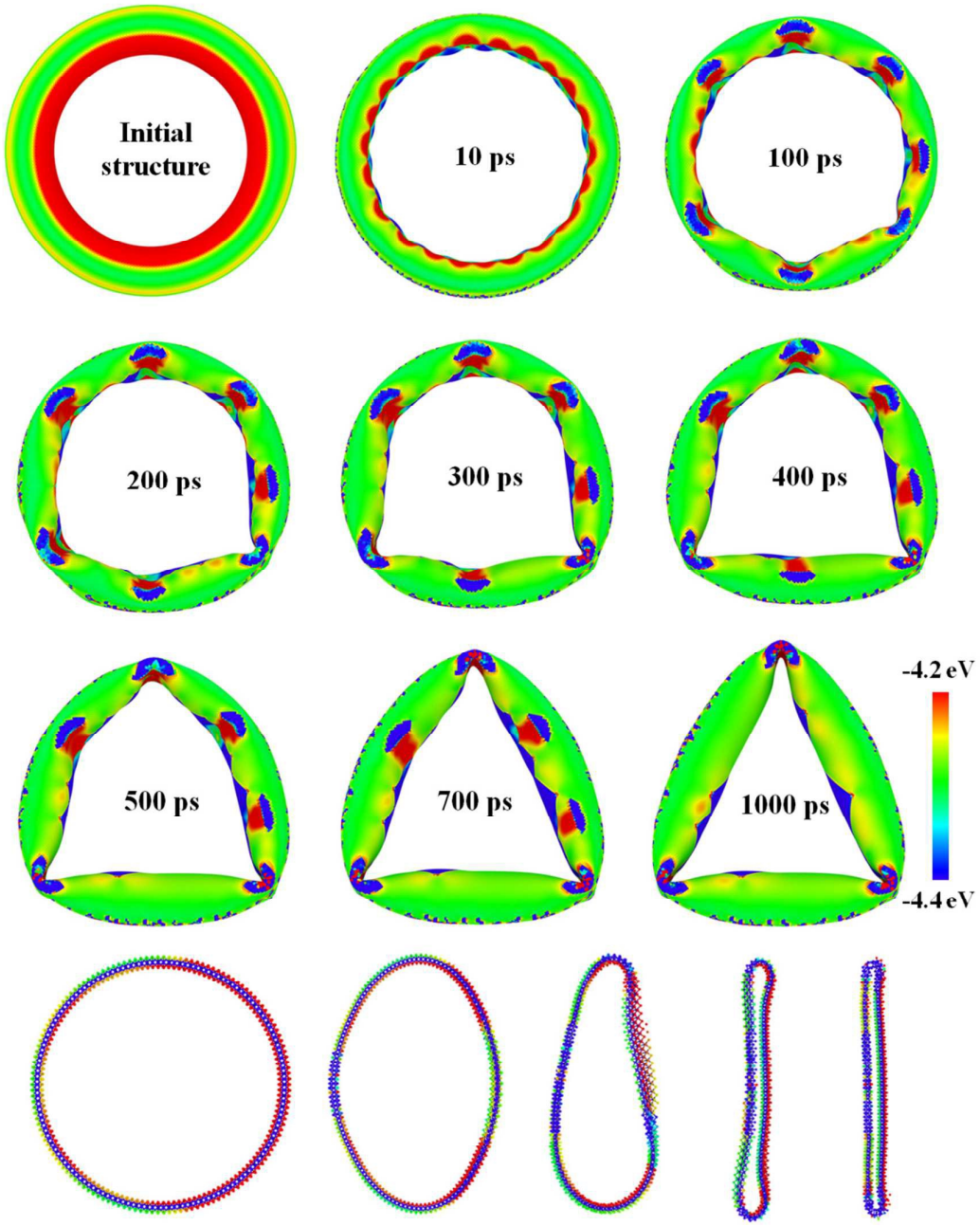

Figure 7

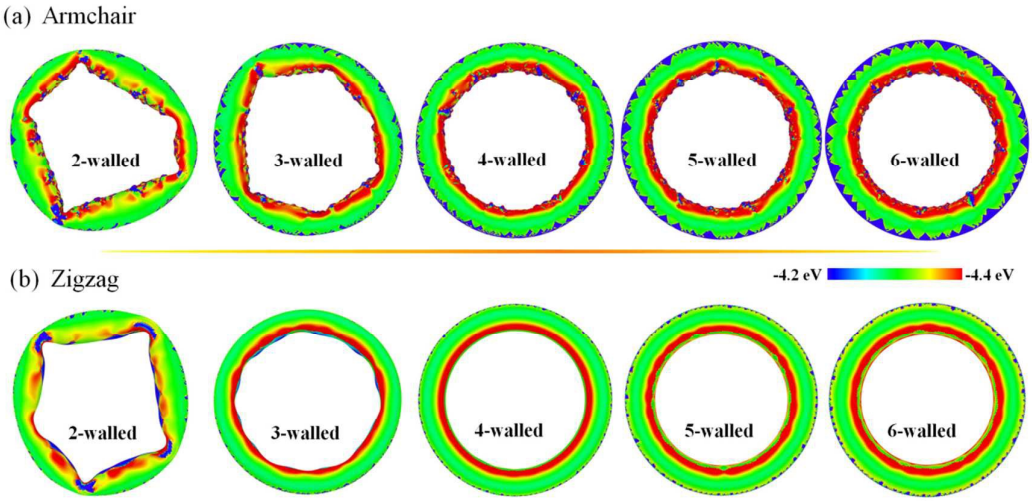

Figure 8

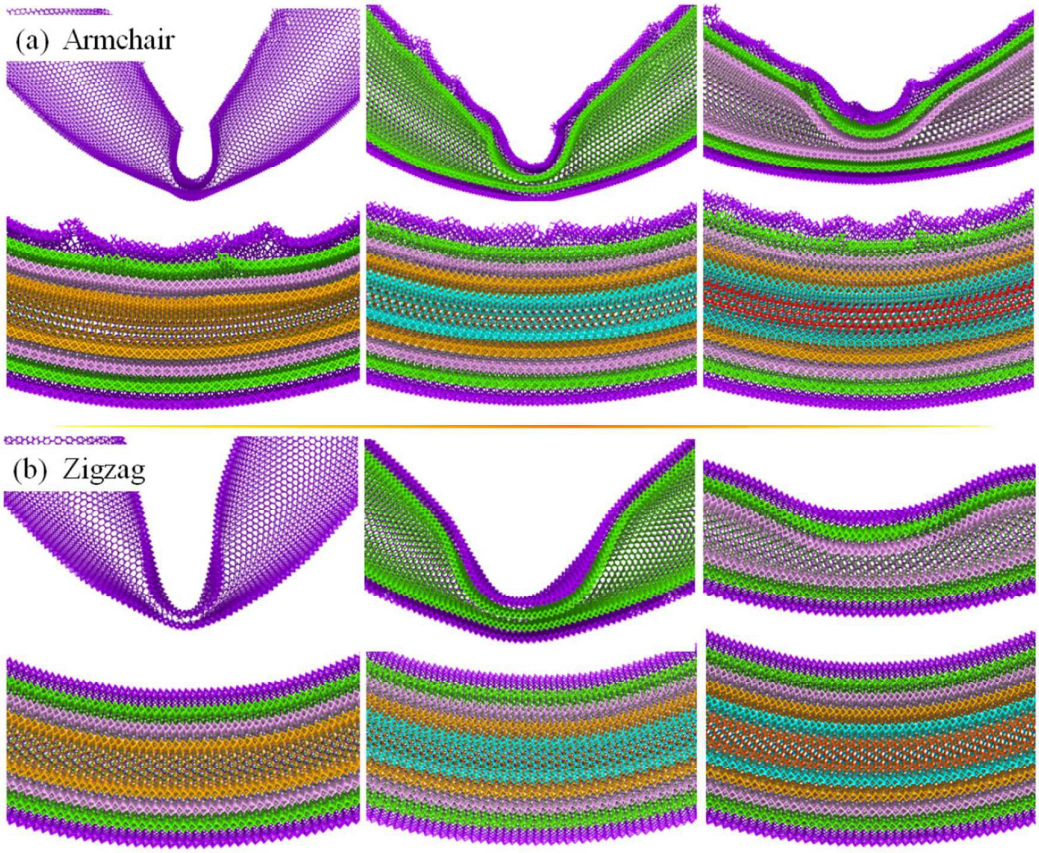

Figure 9

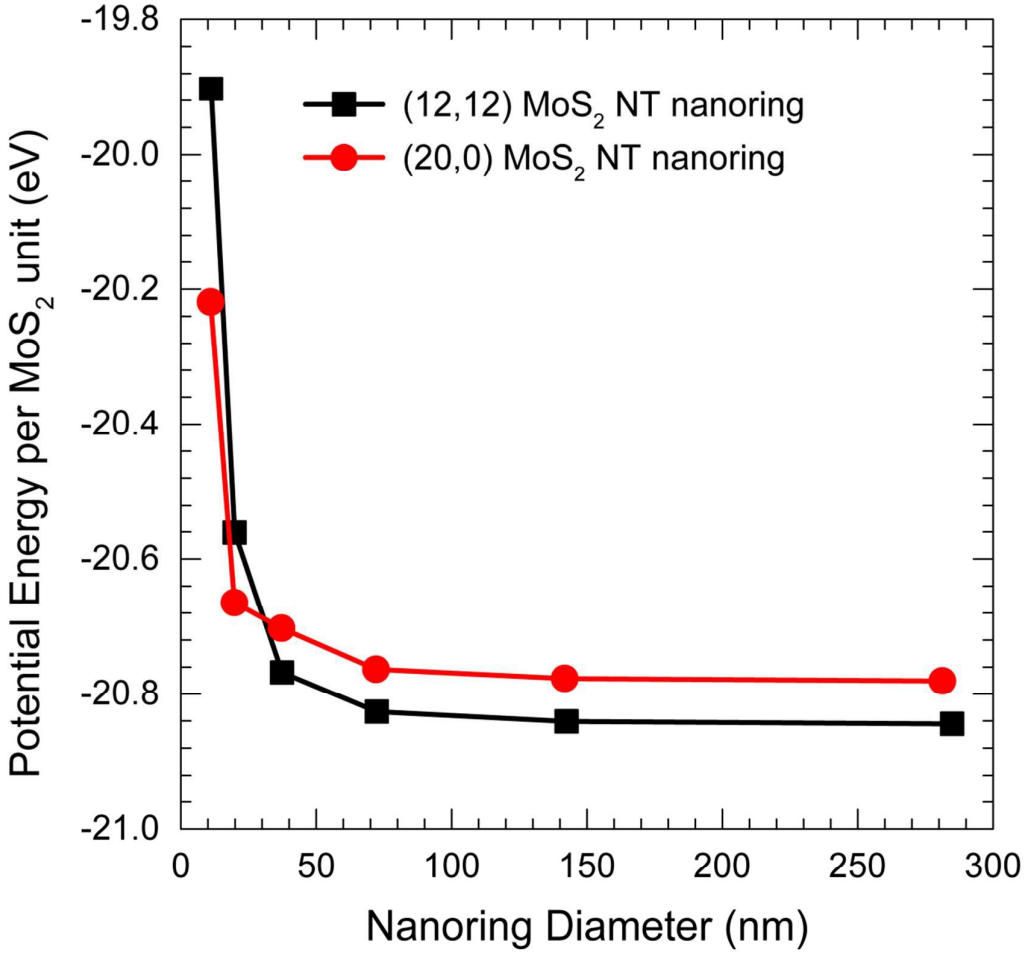

Figure 10

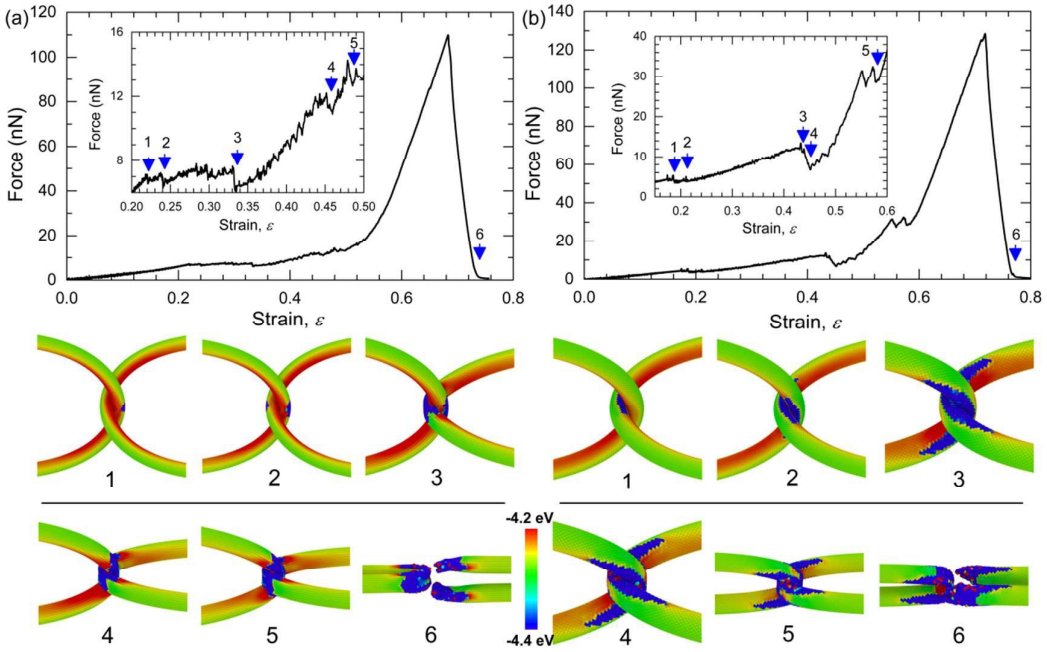

Figure 11

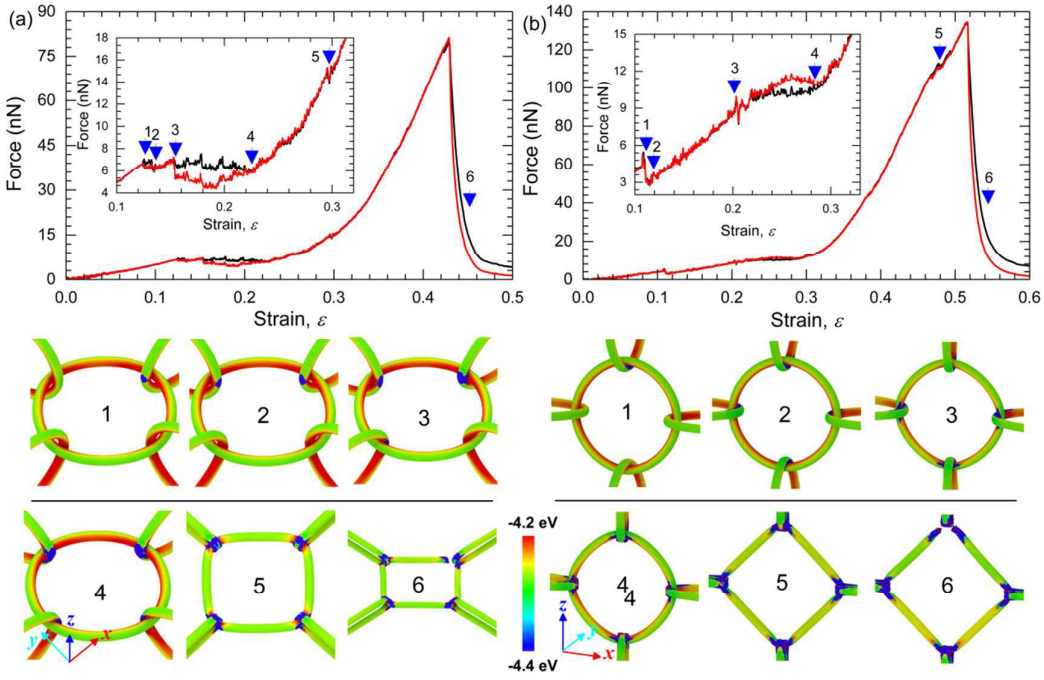

Figure 12

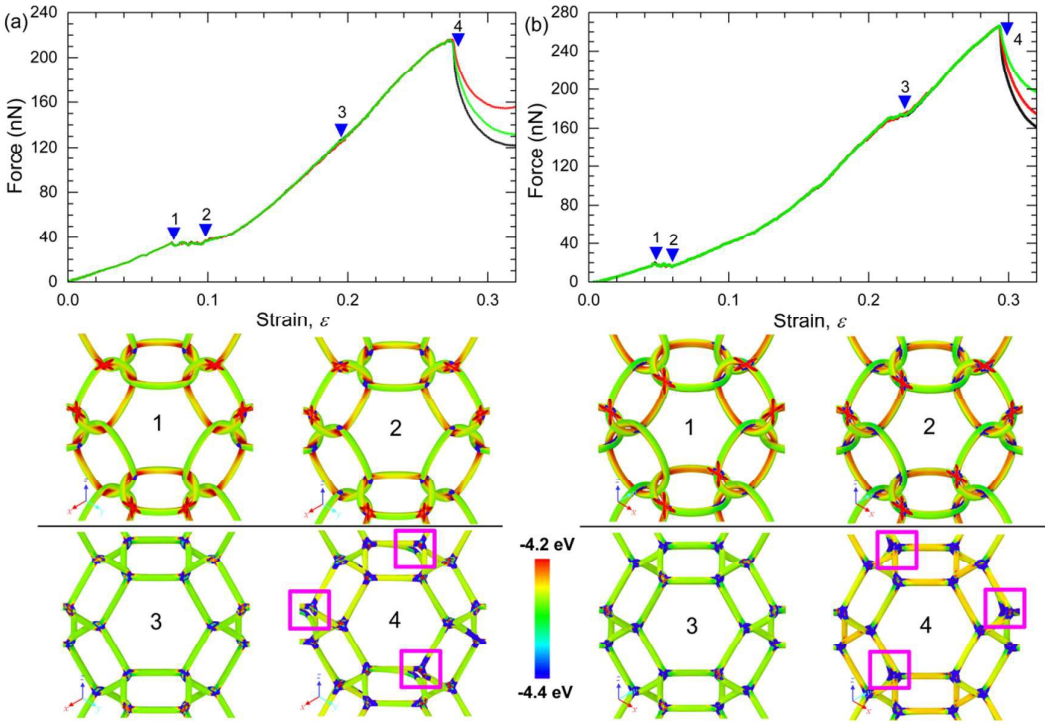

Figure 13